JACS
JOURNAL OF THE AMERICAN CHEMICAL SOCIETY
Article
pubs.acs.org/JACS

Switching Plasmons: Gold Nanorod–Copper Chalcogenide Core–Shell Nanoparticle Clusters with Selectable Metal/Semiconductor NIR Plasmon Resonances

Madathumpady Abubaker Habeeb Muhammed,[†,§] Markus Döblinger,[‡,§] and Jessica Rodríguez-Fernández*[,†,§]

[†]Photonics and Optoelectronics Group, Department of Physics and Center for NanoScience (CeNS), Ludwig-Maximilians-Universität München, Amalienstrasse 54, 80799 Munich, Germany

[‡]Department of Chemistry, Ludwig-Maximilians-Universität München, Butenandtstrasse 5-13 (E), 81377 Munich, Germany

[§]Nanosystems Initiative Munich (NIM), Schellingstrasse 4, 80799 Munich, Germany

Supporting Information

ABSTRACT: Exerting control over the near-infrared (NIR) plasmonic response of nanosized metals and semiconductors can facilitate access to unexplored phenomena and applications. Here we combine electrostatic self-assembly and Cd^{2+}/Cu^{+} cation exchange to obtain an anisotropic core–shell nanoparticle cluster (NPC) whose optical properties stem from two dissimilar plasmonic materials: a gold nanorod (AuNR) core and a copper selenide ($Cu_{2-x}Se$, $x \geq 0$) supraparticle shell. The spectral response of the AuNR@Cu_2Se NPCs is governed by the transverse and longitudinal plasmon bands (LPB) of the anisotropic metallic core, since the Cu_2Se shell is nonplasmonic. Under aerobic conditions the shell undergoes vacancy doping ($x > 0$), leading to the plasmon-rich NIR spectrum of the AuNR@$Cu_{2-x}Se$ NPCs. For low vacancy doping levels the NIR optical properties of the dually plasmonic NPCs are determined by the LPBs of the semiconductor shell (along its major longitudinal axis) and of the metal core. Conversely, for high vacancy doping levels their NIR optical response is dominated by the two most intense plasmon modes from the shell: the transverse (along the shortest transversal axis) and longitudinal (along the major longitudinal axis) modes. The optical properties of the NPCs can be reversibly switched back to a purely metallic plasmonic character upon reversible conversion of AuNR@$Cu_{2-x}Se$ into AuNR@Cu_2Se. Such well-defined nanosized colloidal assemblies feature the unique ability of holding an all-metallic, a metallic/semiconductor, or an all-semiconductor plasmonic response in the NIR. Therefore, they can serve as an ideal platform to evaluate the crosstalk between plasmonic metals and plasmonic semiconductors at the nanoscale. Furthermore, their versatility to display plasmon modes in the first, second, or both NIR windows is particularly advantageous for bioapplications, especially considering their strong absorbing and near-field enhancing properties.

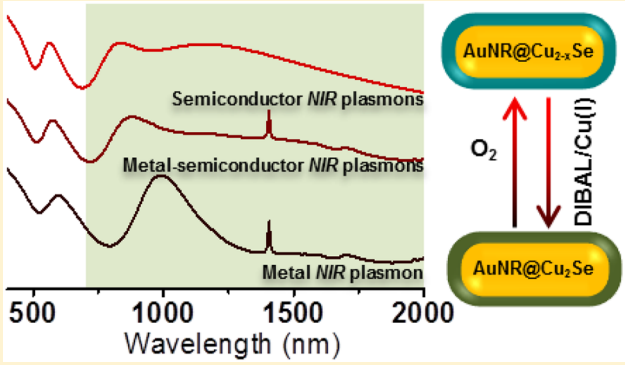

INTRODUCTION

Nanoparticles of noble metals exhibit single or multiple localized surface plasmon resonance (LSPR) bands located in the visible and/or near-infrared (NIR) depending on nanoparticle size, shape, and chemical composition.[1−12] Their plasmon modes arise from the collective oscillation of negatively charged free carriers, specifically electrons. Plasmonic metals find a multitude of applications in all branches of science and technology ranging from nanomedicine[13−17] to catalysis[18,19] and sensing.[20−22] In the past few years nanoparticles made out of doped semiconductors, including vacancy-doped copper chalcogenides ($Cu_{2-x}Y$, $x > 0$, Y = S, Se, Te), have emerged as a new set of plasmonic materials[23−34] and thereby served as the starting point for the rapidly growing field of semiconductor plasmonics. Nonstoichiometric copper chalcogenides exhibit LSPRs in the NIR spectral region due to their charge carrier density levels. Unlike metal nanoparticles, their plasmonic character stems from the collective oscillation of positively charged charge carriers (specifically, holes). Furthermore, while in metallic nanoparticles the plasmon modes are essentially "locked" after synthesis, the LSPR wavelength of vacancy-doped copper chalcogenide nanoparticles can be tuned by adjusting the extent of vacancy doping. Vacancies can be created by several ways, including simple exposure to atmospheric oxygen,[25,35] by addition of an external oxidizing agent,[35] by postsynthetic thermal treatment,[29] or by ligand exchange.[36] Copper chalcogenide nanoparticles can be

Received: May 22, 2015
Published: September 2, 2015

DOI: 10.1021/jacs.5b05337
J. Am. Chem. Soc. 2015, 137, 11666−11677

synthesized either directly from a Cu precursor[25,37] or indirectly by the cation exchange of presynthesized materials like cadmium chalcogenides.[26,38,39] Cation exchange is an age-old technique that can be used to chemically convert preformed nanomaterials into analogue nanomaterials with a different set of cations while keeping the size and shape of the original material intact.[26,39−41] Cation exchange is particularly employed when direct synthesis of certain materials is challenging due to a poor particle size, shape, monodispersity, composition, and stability control.[26]

Plasmonic copper chalcogenide nanoparticles find applications in several areas such as photothermal therapy,[42,43] or bioimaging,[44,45] but also as SERS,[37] and plasmonic probes to study local chemical events.[38] For instance, hydrophilic Cu_9S_5 nanoparticles with a platelet-like structure can be used as photothermal agents with high heat conversion efficiency up to 25.7% to kill cancer cells in vivo due to their NIR plasmon resonance.[43] Ku et al. demonstrated that NIR plasmonic self-doped CuS nanoparticles could act as contrast agents in photoacoustic tomography to visualize mouse brain and rat lymphnodes.[44] In another report by Jain et al. CuS nanorods have been used as a model system of doped-semiconductor-based plasmonic probes.[38] This is based on the tunability of their NIR LSPR due to the change in doping level associated with chemical events such as impurity doping, ligand binding, and electrochemical charging or discharging happening in the vicinity on the nanoparticles. Combining the aforementioned two entirely different types of plasmonic materials (metals and vacancy-doped semiconductors) is of high interest to gain access to unexplored phenomena arising from the interaction of two intrinsically dissimilar plasmonic building blocks. Few reports are present on the formation of gold-doped copper chalcogenide hybrid nanostructures. For instance, Ding et al. devised an Au−Cu_9S_5 hybrid to study the LSPR coupling effect between the two plasmonic components.[46] In spite of their low spectral overlap, a 50% absorption enhancement at 1064 nm was reported due to the presence of the spherical Au component. Additional properties such as low cytotoxicity, high photothermal transduction efficiency, etc., point toward these hybrids as excellent candidates for bioimaging and phototherapy applications. In another report by Liu et al., heavily doped $Cu_{2-x}Se$ nanoparticles were combined with spherical Au nanoparticles to create a new type of hybrid material.[47] These hybrid particles exhibit broad absorption across the visible and NIR and were used for in vivo photoacoustic imaging and in vitro dark-field imaging. To the best of our knowledge, only spherical gold nanoparticles with LSPR in the visible range have been used so far for the preparation of gold−copper chalcogenide hybrid nanosystems. By employing metal nanoparticles with anisotropic shapes, such as AuNRs, the LSPR from the gold component can be pushed into the NIR range, where the LSPR of copper chalcogenides is also centered.

In this work, we used electrostatic self-assembly to obtain a well-defined core−shell NPC consisting of an AuNR core and a supraparticle CdSe shell. We show that the supraparticle shell can undergo Cd^{2+}/Cu^{+} cation exchange and subsequent vacancy doping, thereby yielding a dual metal/semiconductor plasmonic core−shell NPC (AuNR@$Cu_{2-x}Se$) with a plasmon-rich response in the NIR. Unlike previous works where the interfacial contact area between the metal and the vacancy-doped semiconductor is partial, the core−shell morphology of our NPCs enables an intimate contact between the individual plasmonic components over a larger surface area. Our experimental and optical modeling results demonstrate the unique ability of our anisotropic core−shell NPCs to display a reversibly switchable NIR optical response governed by the plasmonic modes of the metallic core, of the metallic core and the semiconductor shell, or of the semiconductor shell alone depending on the vacancy doping level. Such a rich plasmonic behavior for a hybrid metal−semiconductor has not been reported before.

EXPERIMENTAL SECTION

Materials. All chemicals obtained from commercial suppliers were used without further purification. Hydrogen tetrachloroaurate trihydrate ($HAuCl_4·3H_2O$), cetyltrimethylammonium bromide (CTAB), ascorbic acid, sodium borohydride ($NaBH_4$), silver nitrate ($AgNO_3$), sodium hydroxide (NaOH), sodium chloride (NaCl), hydrochloric acid (HCl, 32 wt % in water), cadmium perchlorate hydrate ($Cd(ClO_4)_2·xH_2O$), sodium citrate dihydrate, *N*,*N*-dimethylselenourea, poly(styrene sulfonic acid)sodium (PSS, M_w 70 000 g/mol), octadecylamine (ODA), tetrakis(acetonitrile)copper(I) hexafluorophosphate ($[Cu(CH_3CN)_4]PF_6$), potassium cyanide (KCN), tetrachloroethylene anhydrous (TCE), and methanol anhydrous were purchased from Sigma-Aldrich. Sodium oleate (NaOL) was purchased from TCI America. Methoxy PEG thiol (HS-PEG-MeO, M_w = 5000 Da) was purchased from RAPP polymere. Milli-Q water with a resistivity higher than 18.2 MΩ·cm was used in the experiments. All glassware was cleaned with aqua regia.

Synthesis of AuNRs. Monodisperse AuNRs were synthesized according to the protocol described by Ye et al.[6] using a binary surfactant mixture consisting of cetyltrimethylammonium bromide (CTAB) and sodium oleate (NaOL). The synthesis involves two steps.

Step 1, Preparation of the Seed Solution. A 5 mL amount of an aqueous $HAuCl_4·3H_2O$ (0.5 mM) were mixed with 5 mL of an aqueous CTAB solution (0.2 M). This was followed by addition of 1 mL of a freshly prepared $NaBH_4$ solution (0.6 mL of 0.01 M of $NaBH_4$ was diluted to 1 mL with water) under vigorous stirring. The stirring was stopped after 2 min. Thereafter, the seed solution was allowed to age for 30 min in a water bath at 27 °C.

Step 2, Preparation of the Growth Solution. CTAB (7 g) and NaOL (1.234 g) were dissolved in 250 mL of warm water (∼50 °C). When the solution was cooled down to 30 °C, $AgNO_3$ (4 mM, 18 mL) was added and the solution was kept undisturbed for 15 min at 30 °C. Then an aqueous $HAuCl_4·3H_2O$ solution (1 mM, 250 mL) was added. The solution turned colorless after 90 min of stirring at 700 rpm. This was followed by the addition of 2.499 mL of HCl (32 wt % in water), while stirring was continued for another 15 min at 400 rpm. Thereafter, ascorbic acid (64 mM, 1.25 mL) was added and the solution was stirred vigorously for 30 s. Lastly, 4 mL of the seed solution were also added to the growth solution. After stirring for an additional 30 s, the reaction mixture was stored overnight in a water bath at 30 °C to allow for gold nanorod formation. The NRs were purified by centrifugation at 7000 rpm for 30 min (2×) and redispersed in 250 mL of a 5 mM CTAB solution.

Growth of CdSe Supraparticles (CdSe SPs) on AuNRs. To obtain AuNR@CdSe NPCs we used the method described by Kotov and co-workers.[48] Prior to CdSe deposition, positively charged CTAB-capped AuNRs were coated with the negatively charged PSS polymer. For this, 5 mL of an AuNR dispersion (having [Au] = 0.7 mM and [CTAB] = 2 mM) was added to 5 mL of an aqueous PSS solution (12 mg/mL, 6 mM NaCl) and stirred overnight. The solution was centrifuged at 7000 rpm for 30 min (2×) and redispersed in 5 mL of water. To induce the in situ formation and self-assembly of a CdSe supraparticle shell on the AuNRs surface, 5 mL of AuNR@PSS was diluted to 25 mL with water. This was followed by the addition of 14.75 μmol of sodium citrate, followed by addition of 6.6 μmol of $Cd(ClO_4)_2·xH_2O$. The pH of the solution was adjusted to 9.3 by addition of 100 mM NaOH, and the solution was deaerated by bubbling either N_2 or Ar for 15 min. This was followed by injection of

DOI: 10.1021/jacs.5b05337
J. Am. Chem. Soc. 2015, 137, 11666−11677

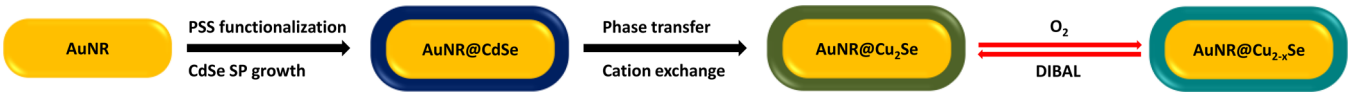

Figure 1. Schematic representation of the synthesis of AuNR@$Cu_{2-x}Se$ ($x \geq 0$) NPCs from AuNR building blocks. In the first step supraparticles comprising CdSe nanoparticles are grown on the surface of PSS-modified AuNRs to form AuNR@CdSe NPCs. This is followed by an aqueous to organic phase transfer and subsequent cation exchange of Cd(II) ions with Cu(I) to form AuNR@Cu_2Se. The plasmonic properties of the AuNR@Cu_2Se/AuNR@$Cu_{2-x}Se$ NPCs can be reversibly tuned under oxidative (O_2)/reductive (DIBAL) conditions.

2.2 μmol of *N*,*N*-dimethylselenourea dissolved in water under vigorous stirring. The resulting solution was heated to 70 °C and refluxed under N_2 or Ar for 12 h. The precursors were added a total of 3 times to obtain shell thicknesses of 12−14 nm.

Cation Exchange of AuNR@CdSe To Form AuNR@Cu_2Se. Cd^{2+}/Cu^{+} cation exchange was carried out in a N_2-filled glovebox. The AuNR@CdSe NPCs were first phase transferred to TCE from water upon surface modification with ODA. For this, 4 mL of an aqueous solution of AuNR@CdSe NPCs was mixed with 4 mL of a 10 mM ethanolic solution of ODA. The NPCs were precipitated as a separate layer at the top of the solution. The solvent mixture was removed carefully with a syringe, and the AuNR@CdSe NPCs were subsequently redispersed in ethanol. To remove the excess of ODA, the ethanolic solution was centrifuged and the precipitated NPCs were finally redispersed in 4 mL of anhydrous TCE inside a glovebox. To perform the cation exchange, 58 μL of a Cu(I) stock solution (consisting of 10 mg of $[Cu(CH_3CN)_4]PF_6$) dissolved in 1 mL of anhydrous methanol) were added to 4 mL of the AuNR@CdSe NPCs under vigorous stirring. We used a 5× stoichiometric excess of Cu(I) for cation exchange. After 2 min of stirring, 2 mL of anhydrous methanol were added and the dispersion was centrifuged at 5000 rpm for 5 min and finally redispersed in TCE.

Reversible AuNR@Cu_2Se ↔ AuNR@$Cu_{2-x}Se$ Conversion. *Conversion of AuNR@Cu_2Se into AuNR@$Cu_{2-x}Se$ upon Air Exposure.* AuNR@Cu_2Se NPCs dispersed in TCE were transferred into a sealed NIR quartz cuvette inside a glovebox. Thereafter, an extinction spectrum was measured (0 min O_2 exposure time) by keeping the cuvette cap tightly closed. Subsequently, the sample was exposed to air by opening the cuvette cap. The spectral changes in the vis−NIR were monitored over time until no further changes were measured.

Conversion of AuNR@$Cu_{2-x}Se$ into AuNR@Cu_2Se. Two different routes were carried out for the conversion of AuNR@$Cu_{2-x}Se$ NPCs into AuNR@Cu_2Se.

Route 1, Reduction by DIBAL Addition. A 10 μL amount of DIBAL (25 wt % in toluene) was added into 2 mL of preoxidized (24 h) AuNR@$Cu_{2-x}Se$ NPCs in a sealed cuvette inside a glovebox. The spectral changes were monitored at various time intervals until a complete suppression of the plasmon bands from the $Cu_{2-x}Se$ shell was observed.

Route 2, Reduction by Cu(I) Addition. A 10 μL amount of $[Cu(CH_3CN)_4]PF_6$ dissolved in anhydrous methanol (10 mg/mL) was added into 2 mL of preoxidized (24 h) AuNR@$Cu_{2-x}Se$ in a sealed cuvette inside a glovebox. The changes in the UV−vis−NIR extinction spectra were monitored over time. Addition of Cu(I) was repeated several times (a total of 60 μL was added) until the complete suppression of the plasmon bands from the $Cu_{2-x}Se$ shell was observed.

PEGylation of AuNR@$Cu_{2-x}Se$ and Water Transfer. In a typical PEGylation experiment, 3 mL of AuNR@Cu_2Se NPCs (stabilized with ODA, in TCE) were first oxidized into AuNR@$Cu_{2-x}Se$ upon air exposure until all plasmon peaks, namely, *LSPR I*, *LSPR III*, and *LSPR IV* (see main text for details), were clearly observed. Subsequently, the sample was centrifuged at 5000 rpm for 5 min. The precipitate was dried using a N_2 gun and finally redispersed in 3 mL of toluene containing 5 mM methoxy PEG thiol (HS-PEG-MeO, M_w = 5000 Da) under sonication. The NPCs were incubated for 5 min. This time was selected as a compromise to allow for efficient surface grafting of the thiolated PEG on the NPCs' surface while minimizing a significant increase in the hole carrier density of the supraparticle $Cu_{2-x}Se$ shell during the process, i.e., to minimize the extent of further plasmon evolution. After this time the dispersion was centrifuged at 5000 rpm for 5 min. The precipitate was dried using a N_2 gun and redispersed in 3 mL of water.

Oxidation of the Gold Core of AuNR@CdSe and AuNR@$Cu_{2-x}Se$. The gold core of an aqueous dispersion of citrate-stabilized AuNR@CdSe NPCs and PEGylated AuNR@$Cu_{2-x}Se$ NPCs was oxidized (etched) using an aqueous stock solution of KCN (1 M). In both cases a ∼75× molar excess of CN^- with respect to the Au concentration was used for complete dissolution of the gold core. The etching process was monitored by UV−vis−NIR spectroscopy.

Instrumentation. UV−vis−NIR extinction spectra were measured using a Cary 5000 UV−vis−NIR spectrophotometer. Screw-capped NIR quartz cuvettes with a path length of 1 cm were used for all measurements. TCE was used as solvent due to its lower absorption in the NIR, as compared to other organic solvents. Transmission electron microscopy (TEM) images, EDX spectra, and elemental mapping were taken at 300 kV with an FEI Titan 80−300 equipped with a Gatan Tridiem and an EDAX ultrathin window Si (Li) EDX detector. Carbon-coated Cu grids were used for characterization of AuNR@CdSe, and carbon-coated Ni grids were used for characterization of AuNR@$Cu_{2-x}Se$ samples. Wide-angle powder X-ray diffraction patterns were collected using a Bruker D8 diffractometer with a Cu Kα X-ray source operating at 40 kV and 40 mA and a Vantec 2000 area detector. The assignment of crystalline phases was based on the reference files in the Powder Diffraction File (PDF-2) database from the International Center for Diffraction Data.

Optical Modeling. The vis−NIR optical properties of the AuNR@$Cu_{2-x}Se$ NPCs were modeled by means of the boundary element method (BEM).[49,50] For this we modeled an AuNR core with dimensions length × width = 69 × 25 and 5 nm tip curvature (as estimated from TEM analysis) encapsulated by a homogeneous copper selenide shell with the very same rod-like shape and tip curvature and having an average thickness of 10 nm. The dielectric properties of the AuNR core were taken from Johnson and Christy.[51] For the copper selenide ($Cu_{2-x}Se$) shell we used the dielectric functions provided by Dorfs et al.,[35] as calculated by Mansour et al. from bulk reflectivity measurements of polycrystalline samples.[52] Since the dielectric data for $Cu_{2-x}Se$ are available only in the 700−1935 nm range, all spectra were calculated in this spectral range. In particular, we calculated the averaged cross section (averaged over 30 angles of light incidence, comparable to the experimental extinction) of a single AuNR@$Cu_{2-x}Se$ NPC with x = 0.1, 0.13, 0.15, and 0.2. The angle-dependent optical response of a NPC with x = 0.13 was determined by calculating the total cross section (comparable to the extinction cross section) of the cluster at specific angles of light incidence (0°, 45°, and 90°) with respect to its major symmetry axis. For particular angles of light incidence (namely, 0° and 90°), these results were compared with the calculated absorption and scattering cross sections. Near-field enhancement calculations were performed upon illumination with a light source whose wavelength matches that of the LSPR maxima at the corresponding angles of light incidence. All calculations were performed assuming that the single NPCs are redispersed in TCE as solvent (refractive index, n = 1.505). For the hollow case (hollow NPCs), we modeled the optical response of an identically sized and shaped NPC containing a TCE core, rather than a gold one. Optical modeling of a SiO_2NR@$Cu_{2-x}Se$ with the same dimensions for the core and shell as in our experiments was also performed by using the dielectric function of silica from Palik.[53]

DOI: 10.1021/jacs.5b05337
J. Am. Chem. Soc. 2015, 137, 11666−11677

RESULTS AND DISCUSSION

To obtain core−shell AuNR@Cu_2Se NPCs with NIR metal/semiconductor plasmonic properties, we first prepared core−shell AuNR@CdSe NPCs by using AuNRs as building blocks. This was followed by exchange of the cationic Cd sublattice by a Cu sublattice to yield AuNR@Cu_2Se (see scheme in Figure 1). A reversible control over the relative contribution from the metal and copper chalcogenide NIR plasmonic properties was attained by controlling the exposure of the cluster to oxidative or reductive conditions (see Figure 1), as we will discuss further below. The AuNR@CdSe NPCs were obtained by in situ formation and assembly of small CdSe nanoparticles into supraparticles on the surface of negatively charged AuNRs, as described by Kotov and co-workers[48] (see Experimental Section for details). The process consists of the addition of sodium citrate and cadmium perchlorate to an aqueous dispersion of poly(styrene sulfonic acid)sodium (PSS) modified AuNRs. In our case the average length × width of the AuNRs used was 69 × 25 nm (see TEM micrograph in the Supporting Information, Figure S1). After adjustment of the pH of the solution to 9.3 and deaeration, an aqueous solution of *N*,*N*-dimethylselenourea was injected under vigorous stirring. The resulting solution was heated to 70 °C and refluxed under N_2 or Ar atmosphere for 12 h. This led to the formation of a thin supraparticle layer of inhomogeneous thickness around the AuNR cores. We controlled the homogeneity and thickness of the shell by repeating this whole process 2 more times. This allowed us to obtain AuNR@CdSe NPCs with a homogeneous shell of 12−14 nm thickness, as shown in the HRTEM image in Figure 2A (see also lower magnification TEM image in Figure S2A, Supporting Information). The HRTEM micrographs of the AuNR@CdSe NPCs also show a lattice spacing of 0.21 and 0.35 nm. These spacings correspond, respectively, to the (220) and (111) planes of the CdSe shell (see XRD pattern in Figure S3, Supporting Information). The XRD pattern contains intense Bragg reflections corresponding to fcc Au from the AuNR cores and weaker and broader diffraction peaks assigned to cubic CdSe. This latter aspect suggests that the crystallinity of the CdSe supraparticle shell is relatively poor in our system, likely due to the relatively low temperature used for shell formation (70 °C).

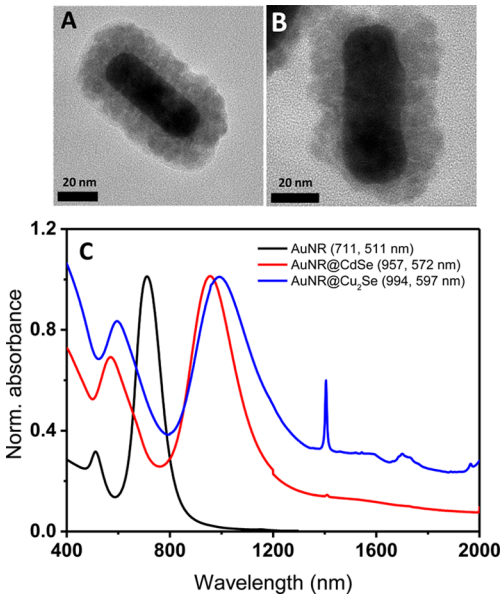

Figure 2. HRTEM images of (A) AuNR@CdSe and (B) AuNR@Cu_2Se NPCs. (C) Extinction spectra of the starting AuNRs (in water, black curve), AuNR@CdSe NPCs (in TCE, red curve), and AuNR@Cu_2Se NPCs (in TCE, blue curve). The spectra are normalized with respect to the corresponding longitudinal plasmon band maximum. The longitudinal and transverse LSPR wavelength maxima of all three samples are shown in the legend.

To perform the cation exchange and thus the conversion of the AuNR@CdSe NPCs into AuNR@Cu_2Se, we first transferred the AuNR@CdSe NPCs from water to tetrachloroethylene (TCE) by modifying the NPCs' surface with octadecylamine (see Experimental Section for details). During this process, the ODA ligands render the NPCs hydrophobic. The geometry, chemical composition, and colloidal stability (see extinction spectra in Figure S4, Supporting Information) of the NPCs remained unaffected during the process. For Cd^{2+}/Cu^{+} cation exchange we redispersed the AuNR@CdSe NPCs in TCE inside a glovebox, followed by the addition of a Cu(I) source, $[Cu(CH_3CN)_4]PF_6$ dissolved in methanol. The color of the colloidal dispersion immediately turned from purple to dark green, suggesting a fast cation exchange. The HRTEM images of the AuNR@Cu_2Se NPCs (see Figure 2B and Figure S2B, Supporting Information) show that the nanorods retain the supraparticle shell, though the thickness varies between 6 and 14 nm. The lower uniformity of the shell after cation exchange is ascribed to a partial disassembly of the supraparticles during the process. Disassembly can be significantly minimized when a 5× Cu^{+} excess with respect to Cd^{2+} is added. These were the conditions used herein (Figure 2B). However, it is the dominant process for a stoichiometric excess >5× (see Figure S5, Supporting Information). From the optical point of view, the changes in the extinction spectra of the NPCs upon cation exchange (see Figure 2C) suggest that the dielectric properties of the semiconductor shell encapsulating the AuNR cores are indeed modified during the process. The starting AuNR@CdSe in TCE exhibit a transverse and a longitudinal plasmon band centered at 572 and 957 nm, respectively. After cation exchange both bands red shift, respectively, to 597 (we will refer to this band as *LSPR I* hereafter) and 994 nm (*LSPR II*). This red shift is ascribed to an increase in the refractive index of the shell and, thus, suggests that the transformation of the CdSe supraparticles into Cu_2Se may have occurred.

In search of further evidence to confirm the exchange of Cd^{2+} by Cu^{+} ions we analyzed the elemental composition of the AuNR@CdSe NPCs before and after cation exchange. The EDX spectra and elemental mapping data of the relevant elements for two representative NPCs before and after cation exchange are shown in Figure 3. The EDX spectrum before cation exchange displayed in Figure 3A shows the presence of elemental Au, Cd, and Se, with a clear distribution of Au in the core, and Cd and Se in the shell (see corresponding elemental maps in Figure S6A, Supporting Information). In contrast, after cation exchange the EDX spectrum shows the presence of Au, Cu, and Se (Figure 3B). The elemental maps indicate a clear distribution of Cu and Se in the shell and Au in the core (see inset of Figure 3B and Figure S6B). We also note that some residual Cd is detected after cation exchange as a very weak Cd_L peak, while the peak corresponding to Cd_K is below the detection limit. This very small amount of Cd detected may be due to the presence of some chemisorbed Cd^{2+} that cannot be efficiently removed from the NPCs' surface, despite thorough

DOI: 10.1021/jacs.5b05337
J. Am. Chem. Soc. 2015, 137, 11666−11677

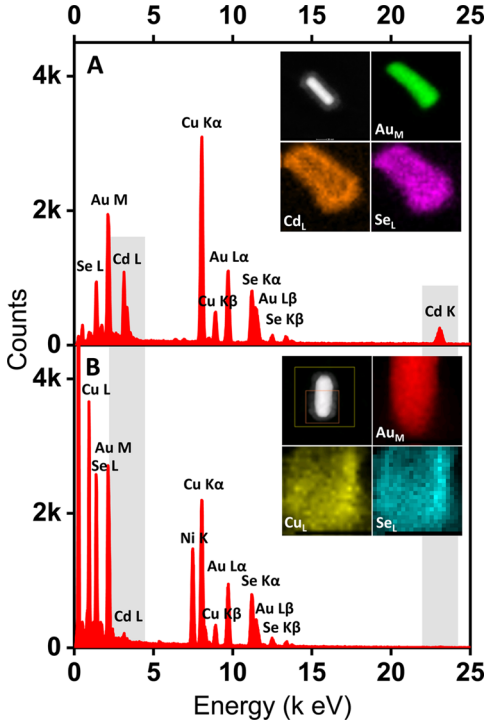

Figure 3. EDX spectra of (A) AuNR@CdSe and (B) AuNR@Cu_2Se NPCs. Elemental maps corresponding to the most intense lines of each element are given as insets. We note here that due to the analysis of AuNR@Cu_2Se in an oxygen-rich environment, vacancy doping of the shell cannot be excluded. Therefore, the sample may be more accurately described as AuNR@$Cu_{2-x}Se$ rather than AuNR@Cu_2Se. Anyhow, this process is not expected to influence the presence of the elements shown in the EDX spectra and elemental maps. Elemental mapping of AuNR@CdSe and AuNR@Cu_2Se was carried out using carbon-coated Cu and Ni TEM grids, respectively, and hence, the presence of Cu and Ni in the corresponding EDX spectra is justified.

washing; it is also detected in EDX measurements on NPC-empty regions of the grid (see Figure S7, Supporting Information). We also performed XRD analysis of the cation-exchanged sample (see Supporting Information, Figure S8), which shows only one set of Bragg reflections corresponding to fcc Au. We have not detected any reflection from the copper selenide shell, likely owing to its low crystallinity. Nevertheless, as we will show below, this is not an issue in terms of the optical response of the system. The most important point herein is that our results demonstrate that Cd^{2+}/Cu^{+} cation exchange can be performed on assemblies of CdSe nanoparticles. To the best of our knowledge, this is the first demonstration of cation exchange on nanoparticle assemblies. It also highlights the importance of finding an optimal ratio between the in- and outgoing cations in order to prevent nanoparticle disassembly during the process (see discussion above and Figure S5).

It is known that stoichiometric copper chalcogenides undergo vacancy doping under aerobic conditions, leading to their transformation into thermodynamically stable non-stoichiometric phases.[25,28,35] Nanoparticles of stoichiometric copper chalcogenides do not exhibit any LSPR due to the absence of charge carriers. However, their nonstoichiometric counterparts are characterized by charge carrier density-dependent NIR plasmon bands.[25,34,35,54] We exposed our AuNR@Cu_2Se NPCs to atmospheric oxygen to create Cu(I) vacancies and charge carriers in the semiconductor supraparticle shell and monitored the process over time by vis−NIR extinction spectroscopy (see Figure 4A). During the first ∼30 min of oxygen exposure, two major changes are observed in the extinction spectrum of the clusters: (i) a continuous blue shift of the transverse (*LSPR I*, see Figure S9A in the Supporting Information) and longitudinal (*LSPR II*) plasmon bands of the AuNR cores, together with a gradual decrease in intensity, especially acute for the *LSPR II* mode, and (ii) the appearance of a new and broad NIR plasmon band (*LSPR III* hereafter), red shifted with respect to *LSPR II*, that gradually blue shifts and increases in intensity. The evolution of the corresponding peak wavelengths for *LSPR I*, *II* (and *IV*, see discussion below), and *III* as a function of oxygen exposure time are summarized in Figure 4B. After exposure for 30 min *LSPR I* shows a ∼24 nm blue shift (from 597 to 573 nm), while for *LSPR II* the blue shift amounts to ∼114 nm (from 994 to 880 nm). At longer O_2 exposure times (>∼30 min) both *LSPR I* and *II* continue blue shifting but at a much slower pace (see Figure 4B) and with their intensity starting to steadily increase. This is a turning point for *LSPR II* since, as will be discussed further below, the plasmon mode *LSPR IV* (see Figure 4A) will dominate the spectral response of the cluster over *LSPR II* at oxidations > 30 min. In the meantime, *LSPR III* continues developing, further blue shifting and gaining intensity, into a well-defined plasmon band. After 46 h under oxidative conditions (red curve in Figure 4A) three plasmon bands centered at ∼563 (*LSPR I*), ∼837 (*LSPR IV*), and ∼1166 nm (*LSPR III*) are clearly identified, with no significant spectral changes observed upon further oxygen exposure up to ca. 3 days.

Electron donors can fill the copper vacancies and decrease the density of holes in the valence band of copper chalcogenides.[38] In our previous work on vacancy-doped copper chalcogenide nanocrystals[25] we showed that with the addition of DIBAL (diisobutylaluminumhydride, a strong reducing agent), electrons can be injected into the semiconductor, thus decreasing the density of holes. Manna et al. demonstrated that nonstoichiometric ($x > 0$) copper chalcogenide nanocrystals can be transformed into stoichiometric ones ($x = 0$) by adding a Cu(I) complex. Herein, we used both DIBAL (Figure 4C and 4D) and a Cu(I) complex (Figure S10, Supporting Information) to decrease the doping level of the supraparticle shell and, thus, transform AuNR@$Cu_{2-x}Se$ into AuNR@Cu_2Se. Figure 4C shows that the optical changes induced on the AuNR@Cu_2Se NPCs upon exposure to oxygen can be fully reverted by adding DIBAL. It has to be noted here that the extinction spectrum of the starting AuNR@$Cu_{2-x}Se$ NPCs shown in Figure 4C (red curve) differs from that of the fully oxidized NPCs shown in Figure 4A (red curve). The AuNR@$Cu_{2-x}Se$ NPCs used for DIBAL reduction belong to a different batch that had been previously exposed to O_2 for only 24 h. This oxidation time was enough to ensure that all three LSPR modes (*I*, *IV*, and *III*) can be easily distinguished prior to DIBAL addition and differs from the longer time oxidation (46 h) used for the NPCs shown in Figure 4A. Two major spectral changes are observed upon addition of DIBAL. First, *LSPR I* and *LSPR IV* red shift during the whole reduction process, with the intensity of *LSPR I* gradually increasing (see Supporting Information Figure S9B) likely due to the presence of residual organics (see TEM micrograph of a DIBAL-treated sample in Figure S11, Supporting Information). However, *LSPR IV* first shows an initial decrease in intensity and a later increase after some time. When the intensity of the mode starts to increase, *LSPR II* becomes the dominant mode over *LSPR*

DOI: 10.1021/jacs.5b05337
J. Am. Chem. Soc. 2015, 137, 11666−11677

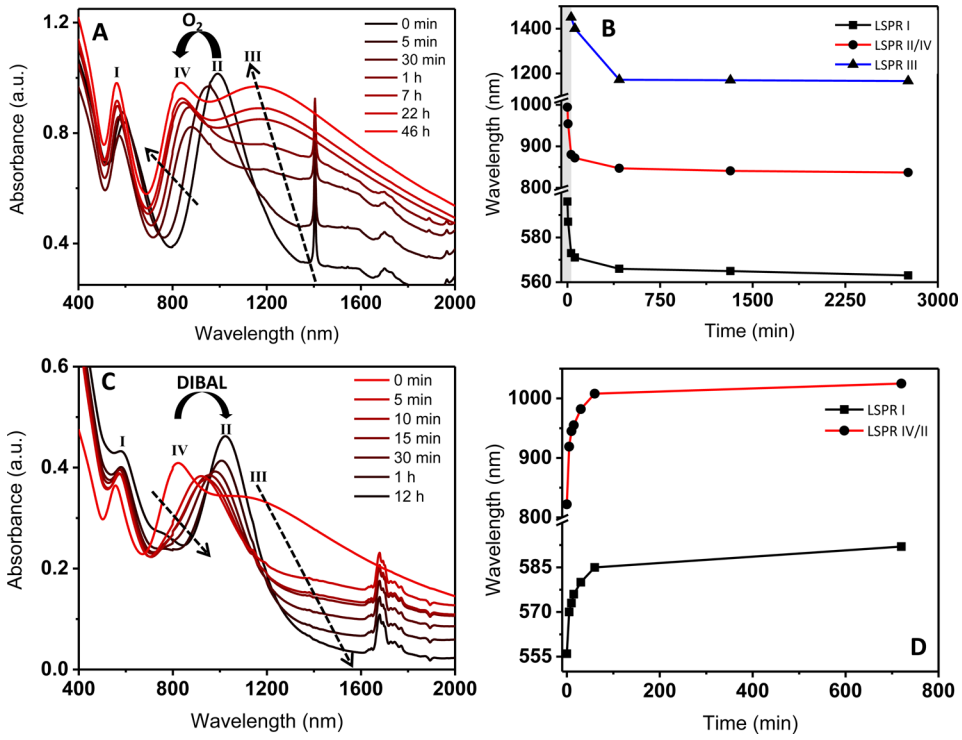

Figure 4. (A) Time-dependent evolution of the vis−NIR extinction spectra of AuNR@Cu_2Se NPCs in TCE during oxidation upon air exposure (the total exposure time from the black to the red curve is 46 h). Plasmon peaks are labeled as *I*, *II*, *III*, and *IV*. (B) Evolution of the plasmon band maximum wavelength for *LSPR I*, *II*, *III*, and *IV* as a function of the O_2 exposure time. The largest blue shift in *LSPR I* and *II* occurs during the first 30 min of oxygen exposure, marked as a gray-shaded area. *LSPR II* is not distinguishable at longer oxidation times since *LSPR IV* is the dominant mode (see discussion following). Since both modes lie around the same spectral region, the evolution of their plasmon band position as a function of oxidation time is plotted as a common red curve in B, with *LSPR II* being the dominant mode during the first 30 min of oxidation (lying within the gray-shaded area) and *LSPR IV* at times > 30 min (outside the gray-shaded area). The red curve clearly illustrates the different blue shifting rate for *LSPR II* and LSPR *IV*, which is due to their different plasmonic origin, as will be discussed below. Note that for *LSPR III* the plasmon peak evolution vs O_2 exposure time is only plotted from 30 min onward since the plasmon band maximum is not clear below 30 min. (C) Spectral evolution of AuNR@$Cu_{2-x}Se$ NPCs (previously exposed to O_2 for 24 h, in TCE) during reduction upon addition of DIBAL, with elapsing exposure time from the red to the black curve. (D) Evolution of the plasmon band maximum wavelength for *LSPR I*, *II*, and *IV* as a function of the DIBAL reduction time. Note that the transition from *LSPR IV* being the dominant mode to *LSPR II* dominating occurs at the time where the red shift starts to occur along with an increase in intensity. As for panel B, the peak position evolution for *LSPR IV* and *II* is plotted in a common red curve. The evolution of *LSPR III* is not included due to the rapid disappearance of the mode upon reaction with DIBAL.

IV, which is not distinguishable anymore. Eventually the mode continues evolving while undergoing a fully reversible evolution as compared to oxidation (see Figure 4A for a qualitative comparison). Second, *LSPR III* gradually red shifts and loses intensity. Upon completion of the process (black curve, Figure 4C), the spectrum of the resulting sample consists of only two plasmon bands, *LSPR I* and *LSPR II*, located at 592 and 1025 nm, respectively, while *LSPR III* has disappeared completely. It has to be noted that upon reduction with strong reducing agents such as DIBAL, the semiconductor shell will reach its most reduced state. This may be the reason for the slight red shift of *LSPR II* when compared to the same sample before oxidation (1025 vs 1020 nm, data not shown). A small absorption profile at ∼770 nm is also visible in the spectrum upon complete reduction with DIBAL (Figure 4C, black curve). This profile is absent when the density of holes in the copper selenide supraparticle shell is reduced upon addition of Cu(I) ions, even though the same spectral changes for *LSPR I*, *IV*, and *III* occur as for DIBAL-assisted reduction (see Figure S10 in the Supporting Information). The ∼770 nm absorption profile may be due to the excitonic peak from the completely reduced Cu_2Se nanoparticles that comprise the supraparticle shell. TEM analysis confirms the overall retention of the Cu_2Se supraparticle shell after reduction with DIBAL (see Figure S11, Supporting Information), though partial disassembly of some shell nanoparticles upon treatment with such a strong reducing agent cannot be fully excluded. We also note here that the kinetics of the DIBAL-induced reduction is much faster than that of the oxygen-induced oxidation. This issue explains the different time windows for both experiment types (see especially Figure 4B and 4D for direct comparison). Overall, our reduction results indicate that, alike vacancy-doped copper chalcogenide nanocrystals, the vacancy-doped supraparticle shell of AuNR@$Cu_{2-x}Se$ NPCs can be reduced, leading to its nondoped AuNR@Cu_2Se NPCs analogue. Furthermore, these results also show that the process is fully reversible, with all plasmon modes undergoing the opposite changes to those reported during aerobic exposure, and ultimately leading to AuNR@Cu_2Se NPCs with identical *LSPR I* and *LSPR II* as those of the starting sample. Moreover, these results also indicate that our AuNR@Cu_2Se NPCs are a reversibly switchable platform for NIR plasmonics.

The interpretation of the plasmon-rich extinction spectra of the AuNR@$Cu_{2-x}Se$ NPCs and of the spectral changes reported in Figure 4 are nontrivial and, therefore, deserve a careful and thorough analysis. To gain more insights into the

DOI: 10.1021/jacs.5b05337
J. Am. Chem. Soc. 2015, 137, 11666−11677

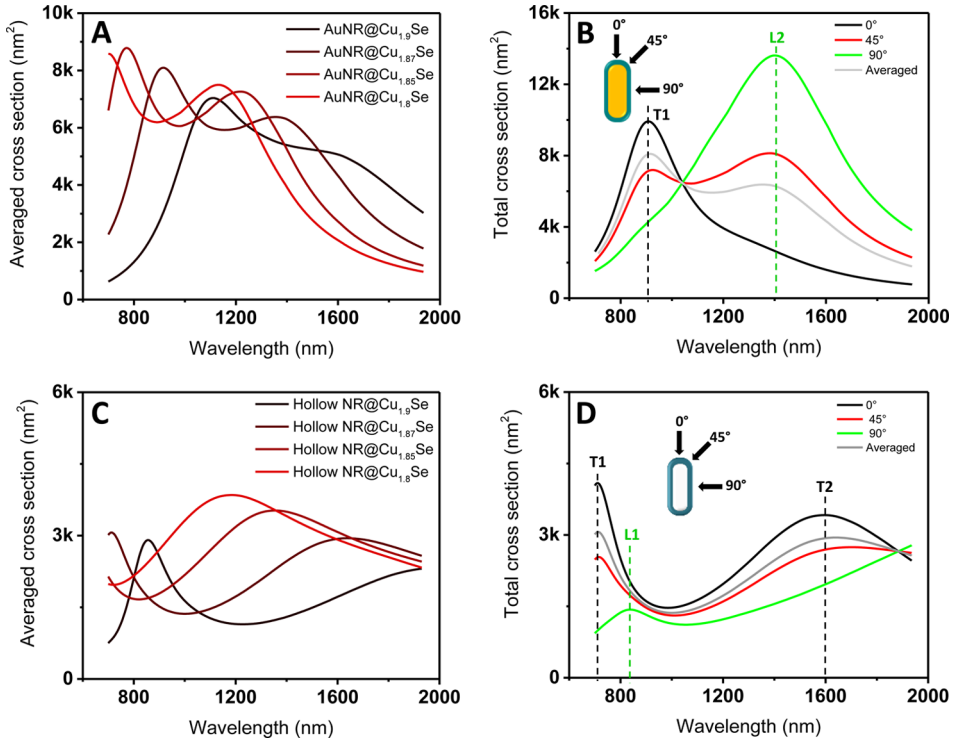

Figure 5. (A) Calculated averaged cross sections for a single AuNR@$Cu_{2-x}Se$ NPC of different stoichiometries given by x = 0.1, 0.13, 0.15, and 0.2 in TCE as solvent. (B) Effect of the angle of light incidence (namely, 0°, 45°, and 90°) on the total cross section of a single AuNR@$Cu_{1.87}Se$ NPC. The calculated averaged cross section (gray curve) is also plotted for comparison. The transverse mode across the shortest axis of the $Cu_{1.87}Se$ shell (T1, 0° incidence) corresponds to *LSPR IV* in the experimental spectra (Figure 4A) for oxidation times > 30 min. The longitudinal mode across the longest axis of the $Cu_{1.87}Se$ shell (L2, 90° incidence) corresponds to *LSPR III* in the experimental spectra (Figure 4A) for oxidation times > 30 min. See discussion for details. (C) Calculated averaged cross sections for a single hollow NR@$Cu_{2-x}Se$ NPC of different shell stoichiometry given by x = 0.1, 0.13, 0.15, and 0.2 in TCE as solvent. Note that the "hollow" terminology is used herein to indicate that gold is not the core material but TCE (the actual solvent used in our experiments). (D) Effect of the angle of light incidence (namely, 0°, 45°, and 90°) on the total cross section of a single hollow NR@$Cu_{1.87}Se$ NPC. The calculated averaged spectrum (gray curve) is shown for comparison. We also note that the spectrum at 45° excitation shows an "intermediate" kind of spectral response, with the modes centered at ∼717 and ∼1700 nm and a clear isosbestic point at ∼1883 nm.

optical properties of our system, we performed optical modeling using the boundary element method (BEM).[49,50] We modeled our core−shell NPCs as an AuNR core (69 × 25 nm, 5 nm tip curvature) encapsulated by a homogeneous rod-shaped copper selenide shell with an average thickness of 10 nm and the same tip curvature as the AuNR core. The dielectric properties of the AuNR core were taken from Johnson and Christy,[51] while the dielectric functions for the copper selenide shell were taken from the data provided by Dorfs et al.,[35] calculated from bulk reflectivity measurements by Mansour et al.[52] We calculated the averaged cross section (comparable to the experimental extinction) of a single AuNR@$Cu_{2-x}Se$ NPC with four different x values (x = 0.1, 0.13, 0.15, 0.2) and using TCE (refractive index, n = 1.505) as solvent. All spectra were calculated in the 700−1935 nm range, where the dielectric data for $Cu_{2-x}Se$ are available. Therefore, our optical modeling discussion will be restricted in the following to *LSPR IV* and *LSPR III*. The calculated spectra for a single AuNR@$Cu_{1.9}Se$, @$Cu_{1.87}Se$, @$Cu_{1.85}Se$, and @$Cu_{1.8}Se$ NPC are shown in Figure 5A. In all cases, the calculated spectra consist of two NIR plasmon bands: a broad mode located at higher wavelengths and a more intense and narrower mode blue shifted with respect to it. The spectral evolution taking place from AuNR@$Cu_{1.9}Se$ (black curve, Figure 5A) to AuNR@$Cu_{1.8}Se$ (red curve, Figure 5A) resembles that of the AuNR@Cu_2Se NPCs upon exposure to oxygen (Figure 4A), with a good qualitative agreement. Both plasmon modes blue shift and increase in intensity with increasing x from AuNR@$Cu_{1.9}Se$ to AuNR@$Cu_{1.8}Se$. The most red-shifted, initially broad, mode in AuNR@$Cu_{1.9}Se$ evolves into a well-defined and narrower plasmon band in AuNR@$Cu_{1.8}Se$. The same occurs for the most blue-shifted mode. The calculated spectra also show that the relative intensity of the lower wavelength mode to the higher wavelength mode gradually decreases as a result of the comparatively larger increase in intensity of the latter from AuNR@$Cu_{1.9}Se$ to AuNR@$Cu_{1.8}Se$. This result is also in qualitative agreement with the experimental spectra shown in Figure 4A, with the intensity ratio *LSPR III*/*LSPR IV* gradually getting close to unity with increasing oxygen exposure time. Therefore, we can conclude that the most red-shifted mode in Figure 5A corresponds to *LSPR III* in Figure 4A and that the most blue-shifted mode in Figure 5A corresponds to *LSPR IV* in Figure 4A. However, it is obvious that this good qualitative agreement between calculated and experimental spectra only holds for the comparison after >30 min oxygen exposure, i.e., when the blue shift of the original *LSPR II* mode occurs along with an increase in intensity, i.e., when *LSPR IV* is the dominant mode. The spectral evolution for *LSPR II* (blue shift and decrease in intensity) for exposures below 30 min is not reproduced in the calculated spectra. Therefore, we will focus first on elucidating the actual origin and mode assignment of *LSPR IV* and *LSPR III* in the >30 min scenario. The

DOI: 10.1021/jacs.5b05337
J. Am. Chem. Soc. 2015, 137, 11666−11677

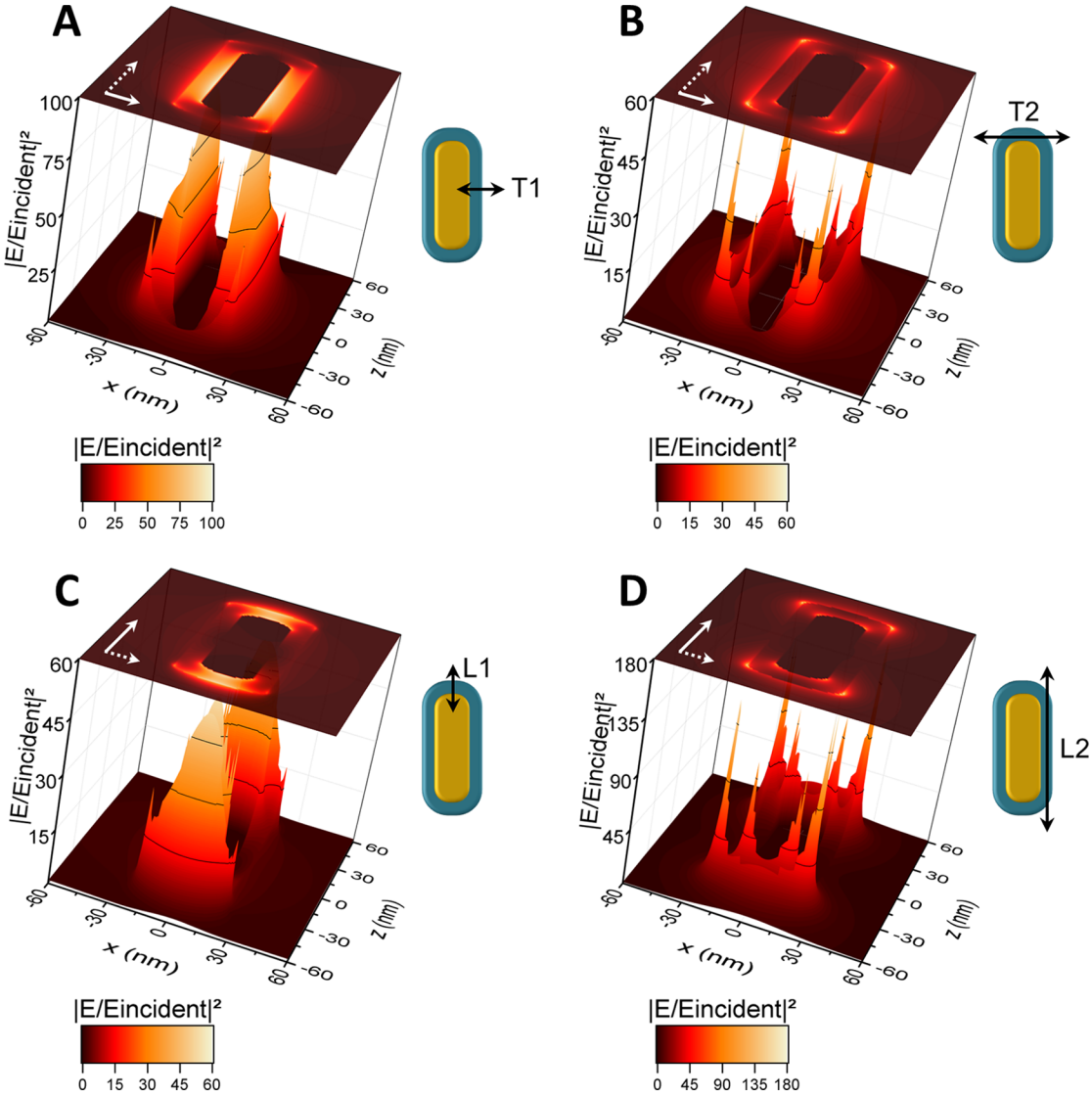

Figure 6. Near-field enhancement maps of an AuNR@$Cu_{1.87}$Se NPC upon illumination with a light beam at (A) 908 (T1), (B) 1275 (T2), (C) 895 (L1), and (D) 1401 nm (L2). In each case the incoming light is represented by a dashed white arrow, while the incident electric field is represented by a solid white arrow. The sketches depict the mode that gets correspondingly excited in each case. Note that the maximum $|\mathbf{E}/\mathbf{E}_{incident}|^2$ for the color gradient bars is not the same for all graphs.

understanding gained will be used subsequently for the interpretation of the spectral changes occurring <30 min.

Given the anisotropic character of our clusters, we calculated the total cross section (comparable to the extinction cross section) of a single AuNR@Cu_{2-x}Se NPC at different angles of light incidence to gain insights into the angular dependence of *LSPR IV* and *LSPR III*. The results for an AuNR@$Cu_{1.87}$Se NPC upon light incidence at 0°, 45°, and 90° with respect to the major axis of the NPC are shown in Figure 5B. The calculated averaged cross section (gray curve) is also included for comparison. When going from 0° to 90° light incidence the relative intensity of *LSPR III* with respect to *LSPR IV* increases. At 0° incidence, transverse plasmon excitation occurs, while at 90° incidence, longitudinal plasmon resonances get excited. The calculated spectrum at 0° light incidence is characterized by an intense transverse mode at ~908 nm (T1 hereafter) and a weak shoulder at ~1275 nm (T2). On the other hand, the calculated spectrum at 90° light incidence shows the presence of a weak longitudinal plasmon resonance (shoulder at ~895 nm, L1 hereafter) and an intense and broad plasmon mode centered at ~1401 nm (L2). By comparing the plasmon modes present in the calculated averaged spectrum (namely, *LSPR IV* at ~915 nm and *LSPR III* at ~1354 nm) with the modes present in the spectra calculated at different angles of light incidence, it seems quite clear that *LSPR IV* is dominated by the contribution from the transverse mode T1 (though having a weak L1 character), while the spectral response of *LSPR III* originates mainly from the longitudinal mode L2 (and has a weaker T2 character). Furthermore, the simulation results in Figure S12 of the Supporting Information also show that both modes are mainly due to light absorption, rather than to scattering.

The calculated spectra for an identical core−shell NPC having the same rod-shaped though hollow (TCE) core are depicted in Figure 5C and 5D and are almost identical to those shown in Figure S13 (Supporting Information) for a SiO_2NR@ Cu_{2-x}Se NPC due to the very similar dielectric function of both dielectric core materials (TCE and silica). In all cases the

DOI: 10.1021/jacs.5b05337
J. Am. Chem. Soc. 2015, 137, 11666−11677

hollow clusters display a broad mode at higher wavelengths and a sharper, more intense mode at lower wavelengths, resembling the calculated spectra of an AuNR@$Cu_{2-x}Se$ NPC (Figure 5A). Also, similarly to the spectra in Figure 5A, both modes blue shift with increasing charge carrier density from $Cu_{1.9}Se$ to $Cu_{1.8}Se$, and the increase in charge carrier density seems to have a stronger impact, in terms of a larger relative blue shift and relative increase in intensity, on the higher wavelength mode. The angle-dependent spectral response of a single hollow and rod-shaped $Cu_{1.87}Se$ shell is shown in Figure 5D. At 0° light incidence (black curve) transverse plasmon modes are excited and the spectrum is characterized by one mode centered at 712 nm (T1 hereafter) and another one at 1595 nm (T2 hereafter). At 90° light incidence (green curve in Figure 5D) longitudinal plasmon modes get excited. In this case the calculated spectrum shows the presence of two modes centered at 836 (hereafter L1, across the shortest longitudinal shell axis) and >2000 nm (L2, across the major longitudinal shell axis, which falls out of the spectral range for which we have dielectric data for the copper chalcogenide shell). These results allow us to understand the angle-averaged spectrum displayed in Figure 5D for a $Cu_{1.87}Se$ shell, as well as the spectra displayed in Figure 5C for all four shell stoichiometries. The sharper higher energy mode in the averaged spectra (Figure 5C) is dominated by the contribution from the transverse mode T1 of the shell, while the broader lower energy mode is dominated by the contribution from the transverse mode T2, at least for the $Cu_{1.87}Se$ case, where the asymmetry of the mode toward higher wavelengths is likely due to the contribution from the L2 mode.

The comparison of the results shown in Figure 5A and 5B for an AuNR@$Cu_{2-x}Se$ NPC and Figure 5C and 5D for a hollow NR@$Cu_{2-x}Se$ NPC allows us to elucidate the effect of the Au NR core in the optical properties of our clusters. In the 700−1935 nm spectral range, the averaged extinction cross section of the AuNR@$Cu_{1.87}Se$ NPC is governed by the shell modes T1 and L2 (Figure 5B). In contrast, the shell modes T1 and T2 dominate the averaged optical response of an identical hollow cluster (Figure 5D). Another effect from the AuNR core relates to the overall extinction cross section of the AuNR@$Cu_{1.87}Se$ NPC, which is larger than that of the hollow cluster throughout the whole 700−1935 nm range. Furthermore, the calculated spectra for various individual clusters consisting of a low aspect ratio (2−2.76) AuNR core of the same width as in our experiments (25 nm) and encapsulated by a 10 nm $Cu_{1.87}Se$ shell point toward a low plasmonic coupling (if any) between the longitudinal plasmon mode of the AuNR core and the T1 mode of the copper selenide shell (see Figure S14 and associated discussion), and also between the longitudinal plasmon mode of the AuNR and the mode L2 of the shell due to their low spectral overlap. These results are in agreement with recent work by Gordon et al. and Ye et al. on Au/In_2O_3[55] and Au/In-doped CdO[56] heterodimers, respectively. In those works a negligible plasmon coupling between the metal and the semiconductor heterodimer units was reported as a consequence of the large energy difference between the plasmon resonances of both materials.

The near-field enhancement (NFE) calculations at each LSPR maxima further support the transverse and longitudinal character of each mode, see Figure 6 for an AuNR@$Cu_{1.87}Se$ NPC and Figure S15 for comparison with the hollow case. The NFE maps upon excitation at T1 (~908 nm) and T2 (~1275 nm) are shown in Figure 6A and Figure 6B, respectively. The maps upon excitation at L1 (~895 nm) and L2 (~1401 nm) are displayed in Figure 6C and 6D. Several aspects can be derived from these results. First, they confirm the transverse character of T1 and T2 and the longitudinal character of L1 and L2. They also allow us to confirm that T1 arises mostly from the excitation of the transverse plasmon mode of the $Cu_{1.87}Se$ shell across the shortest transversal direction, with the maximum enhancement ($|\mathbf{E}/\mathbf{E}_{incident}|^2 \approx 100$) occurring at the metal−semiconductor interface (see Figure 6A and inset sketch). Conversely, T2 is mostly due to the excitation of the transverse mode across the longest transverse direction, with the highest electric field enhancement ($|\mathbf{E}/\mathbf{E}_{incident}|^2 \approx 60$) highly localized at the "external corners" of the $Cu_{1.87}Se$ shell, though with a non-negligible enhancement ($|\mathbf{E}/\mathbf{E}_{incident}|^2 \approx 30$) confined at the "internal shell corners" (see Figure 6B and inset sketch). The picture is identical for L1, which is mainly due to the excitation of the longitudinal plasmon mode of the shell across its shortest longitudinal axis (see Figure 6C), and for L2, which originates mostly from the excitation of the longitudinal plasmon mode of the shell across its longest longitudinal axis (Figure 6D). In the latter case the maximum electric field amplification ($|\mathbf{E}/\mathbf{E}_{incident}|^2 \approx 180$) is highly localized at the "external corners" of the $Cu_{1.87}Se$ shell, while the highly localized amplification ($|\mathbf{E}/\mathbf{E}_{incident}|^2 \approx 90$) at the "internal shell" corners is remarkable as well. The mode assignment made herein is also in agreement with the relative wavelength of each mode (see Figure 5B) and follows the trend L1 ≈ T1 (due to the similar shell thickness across the shortest longitudinal and transverse shell axes) < T2 < L2. The NFE maps also show that the modes L2 and T1 are responsible, respectively, for the highest and second highest electric field enhancements in the AuNR@$Cu_{1.87}Se$ NPC that we modeled. These NFE results also denote the especially high sensitivity of the modes L2 and T1, which are, in turn, the dominant modes in Figure 5A and in our experiments at >30 min oxidation (see Figure 4A). Furthermore, they also indicate that the metal/semiconductor interface is the location where the crosstalk of the two dissimilar plasmonic materials comprising such type of clusters can take place. This is of importance for the rational design of core−shell NPCs where the plasmonic metal core can truly interact with the plasmonic semiconductor shell.

Thus far, we confirmed that *LSPR IV* and *LSPR III* correspond, respectively, to modes T1 and L2 in the >30 min oxygen exposure scenario (Figure 4A). Therefore, the gradual blue shift and increase in intensity for *LSPR IV* (namely, T1) after this exposure time stems from the gradual increase in charge carrier density of the shell upon vacancy formation.[25,28,35] However, the spectral evolution in this region for oxidation times < 30 min involves a gradual plasmon blue shift along with a decrease in intensity. Below 30 min the $Cu_{2-x}Se$ shell is not sufficiently vacancy-doped, and therefore, its transverse plasmon band T1 (*LSPR IV*) is not spectrally visible yet. The longitudinal plasmon band of the AuNRs (*LSPR II*) dominates the spectral response of the cluster in these initial oxidation stages. Hence, the initial blue shift and intensity decrease of *LSPR II* is the result of the sensitivity of the longitudinal plasmon band of the AuNR core to the local dielectric changes occurring on the supraparticle shell in the initial stages of vacancy formation. Once the shell is sufficiently vacancy doped (~30 min), the longitudinal plasmon band of the AuNRs overlaps with the transverse mode (T1) of the shell. This is a turning point for *LSPR II*, as for oxidation times > 30 min its spectral response is not anymore determined by the longitudinal plasmon band of the metal but by the transverse

DOI: 10.1021/jacs.5b05337
J. Am. Chem. Soc. 2015, 137, 11666−11677

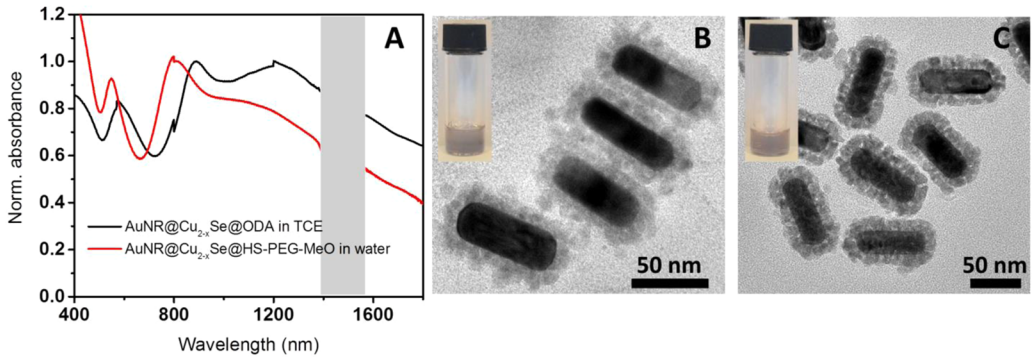

Figure 7. (A) Vis−NIR extinction spectra of AuNR@$Cu_{2-x}Se$ NPCs as oxidized in TCE (black curve) and after PEGylation in toluene and subsequent redispersion in water (red curve). The spectra are normalized at the *LSPR IV* maximum for comparison purposes. The gray shading aims at hiding the high absorption of water in the ca. 1385−1570 nm range. Note that the ligands stabilizing the clusters are octadecylamine in the TCE case and HS-PEG-MeO in the water one. The electron-donating ability of the thiol can explain the slight damping of *LSPR III* in water (see discussion in the main text). TEM micrographs of the NPCs whose spectra are shown in panel A: (B) AuNR@$Cu_{2-x}Se$ in TCE and (C) PEGylated AuNR@$Cu_{2-x}Se$ in water along with a photograph of each colloidal dispersion.

mode T1 of the semiconductor shell, i.e., by *LSPR IV*. It also explains the increase in symmetry and narrowing of the mode (*LSPR IV*) after 30 min oxidation. All these changes, i.e., the evolution from *LSPR II* to *LSPR IV*, are completely reversible, though at a different rate, upon treatment with DIBAL or Cu(I) ions (see Figure 4C and Figure S10). In summary, we demonstrated that the AuNR@$Cu_{2-x}Se$ NPCs prepared herein can be used as a reversibly switchable platform for NIR plasmonics, and they can display NIR plasmon modes being solely due to the anisotropic metal core, to both the metal core and the vacancy-doped semiconductor shell, or to the shell alone. The possibility to control the plasmonic origin of the NIR modes within a nanosized NPC can serve as a starting point to evaluate the plasmonic crosstalk between plasmonic metals and plasmonic semiconductors at the nanoscale. This aspect together with the high spectral tunability of the system across the first and second NIR windows highlights the potential of this dual plasmonic system for biomedical applications. As a first step toward their utilization in the biomedical field we show in Figure 7 that the AuNR@$Cu_{2-x}Se$ NPCs can be successfully transferred from TCE to aqueous medium upon PEGylation with HS-PEG-MeO (see Experimental Section for details). The extinction spectra in Figure 7A show that all three plasmon modes blue shift when transferring the NPCs from TCE to water: from 583 to 547 nm for *LSPR I*, from 887 to 804 nm for *LSPR IV*, and from 1208 to 1080 nm for *LSPR III*. The blue shift of all modes occurs as a result of the lower refractive index of water (1.333) as compared to TCE (1.505). This experimental blue shift is in agreement with the optical modeling results shown in Figure S16, Supporting Information. However, the slight damping of *LSPR III* observed experimentally is not reproduced in the simulated spectra. It is likely that such a damping is due to the electron-donating ability of thiols since HS-PEG-MeO is the ligand stabilizing the NPCs in water. This may result in a slight reduction in hole density of the $Cu_{2-x}Se$ shell and, thus, in a decrease in intensity of the most sensitive plasmon band (*LSPR IV*), as reported elsewhere for other ligands and copper chalcogenide nanocrystals.[36,38,57,58] The TEM micrographs and photographs of each colloidal dispersion further confirm that the water transfer process upon PEGylation yields very stable AuNR@$Cu_{2-x}Se$ NPCs that clearly preserve their supraparticle shells. Having a PEGylated surface, it may be feasible to readily redisperse these NPCs in biological buffers so that their stability and biomedical potential can be effectively assessed. Furthermore, water is also a suitable medium for carrying out the cyanide-assisted oxidation of the AuNR cores. This is of importance for a direct experimental assessment of the role of AuNR cores on the optical response such type of clusters upon comparison with their hollow analogues. First oxidation experiments (see Figure S17) indicate that the $Cu_{2-x}Se$ supraparticle shell disassembles during the process, though it is likely that under milder gold oxidation conditions this issue can be effectively overcome.

■ CONCLUSIONS

Through the combination of electrostatic self-assembly and cation exchange we synthesized an anisotropic, rod-shaped, NPC with core−shell morphology comprising two dissimilar building blocks: a gold nanorod core and a copper selenide supraparticle shell. We demonstrated that the NIR plasmonic behavior of the NPCs can be reversibly switched under oxidative and reductive conditions so that the metal core alone, the metal core and the semiconductor shell, or the shell alone dominate the NIR plasmonic response of the assembly. In the absence of oxygen, the extinction spectrum of the AuNR@Cu_2Se NPCs is all metallic in character, being characterized by the characteristic transverse and longitudinal plasmon bands of the AuNR cores. However, under aerobic conditions the NPCs are characterized by a plasmon-rich spectrum due to the formation of vacancies in the copper chalcogenide shell ($Cu_{2-x}Se$) whose origin we elucidated by means of optical modeling. In the initial stages of exposure to oxidative conditions the NIR spectral response of the NPCs has a dual plasmonic metal/plasmonic semiconductor character given that the level of vacancy doping of the shell is not yet enough to solely dominate the spectral response of the NPCs. Therefore, the extinction spectrum of the NPCs is characterized by the longitudinal plasmon band of the AuNR cores and by a broad, red-shifted, plasmon band (L2), that is mostly due to plasmon excitation along the major longitudinal axis of the copper selenide shell. Conversely, when the level of oxidation is high enough to induce a significant level of vacancy doping on the semiconductor shell, the longitudinal plasmon band of the AuNRs is not distinguishable anymore due to the gradually overlapping and ultimately dominating transverse mode of the

DOI: 10.1021/jacs.5b05337
J. Am. Chem. Soc. 2015, 137, 11666−11677

shell (T1), which is mostly due to plasmon excitation along its shortest transverse axis. Therefore, at longer oxidation times the modes L2 and T1 from the semiconductor shell prevail and dominate the overall NIR response of the AuNR@$Cu_{2-x}Se$ NPCs. We foresee an important potential for such nanosized NPCs in several fields. On one hand, they may serve as a suitable platform to investigate the plasmonic crosstalk between two dissimilar plasmonic materials, namely, metals and semiconductors. Moreover, several phenomena of interest for photovoltaics and photocatalysis, such as electron injection, may be investigated with this system. The light-absorbing properties of our NPCs can also be of special interest in the biomedical field, for instance, for photothermal therapy, especially due to the possibility they offer to span both the first and the second NIR windows, and also for theranostics, given the high electric field enhancements at the metal–semiconductor interface.

■ ASSOCIATED CONTENT

Supporting Information

The Supporting Information is available free of charge on the ACS Publications website at DOI: 10.1021/jacs.5b05337.

Additional TEM images, XRD patterns, optical characterization, elemental mapping, STEM, EDX, optical modeling results, and experiments (PDF)

■ AUTHOR INFORMATION

Corresponding Author

*Jessica.Rodriguez@lmu.de

Notes

The authors declare no competing financial interest.

■ ACKNOWLEDGMENTS

We acknowledge funding from the European Union's Seventh Framework Programme for research, technological development, and demonstration under grant agreement No. 310250 (project UNION) and from the LMU Excellent Junior Researcher Fund (project HE-Go-3D) within the DFG-funded Excellence Initiative. We also thank Katja Lyons for technical assistance with HRTEM measurements.

■ REFERENCES

(1) Hiramatsu, H.; Osterloh, F. E. *Chem. Mater.* **2004**, *16*, 2509.
(2) Bastús, N. G.; Merkoçi, F.; Piella, J.; Puntes, V. *Chem. Mater.* **2014**, *26*, 2836.
(3) Yu, D. B.; Yam, V. W. W. *J. Am. Chem. Soc.* **2004**, *126*, 13200.
(4) Gou, L. F.; Murphy, C. J. *Chem. Mater.* **2005**, *17*, 3668.
(5) Barbosa, S.; Agrawal, A.; Rodríguez-Lorenzo, L.; Pastoriza-Santos, I.; Álvarez-Puebla, R. A.; Kornowski, A.; Weller, H.; Liz-Marzán, L. M. *Langmuir* **2010**, *26*, 14943.
(6) Ye, X. C.; Zheng, C.; Chen, J.; Gao, Y. Z.; Murray, C. B. *Nano Lett.* **2013**, *13*, 765.
(7) Eustis, S.; El-Sayed, M. A. *Chem. Soc. Rev.* **2006**, *35*, 209.
(8) Daniel, M. C.; Astruc, D. *Chem. Rev.* **2004**, *104*, 293.
(9) Rodríguez-Fernández, J.; Pérez-Juste, J.; de Abajo, F. J. G.; Liz-Marzán, L. M. *Langmuir* **2006**, *22*, 7007.
(10) Rodríguez-Fernández, J.; Pastoriza-Santos, I.; Pérez-Juste, J.; de Abajo, F. J. G.; Liz-Marzán, L. M. *J. Phys. Chem. C* **2007**, *111*, 13361.
(11) Oh, E.; Susumu, K.; Goswami, R.; Mattoussi, H. *Langmuir* **2010**, *26*, 7604.
(12) Blanch, A. J.; Döblinger, M.; Rodríguez-Fernández, J. *Small* **2015**, DOI: 10.1002/smll.201500095.
(13) El-Sayed, I. H.; Huang, X. H.; El-Sayed, M. A. *Nano Lett.* **2005**, *5*, 829.
(14) Sperling, R. A.; Rivera-Gil, P.; Zhang, F.; Zanella, M.; Parak, W. J. *Chem. Soc. Rev.* **2008**, *37*, 1896.
(15) Pissuwan, D.; Niidome, T.; Cortie, M. B. *J. Controlled Release* **2011**, *149*, 65.
(16) Ghosh, P.; Han, G.; De, M.; Kim, C. K.; Rotello, V. M. *Adv. Drug Delivery Rev.* **2008**, *60*, 1307.
(17) Dreaden, E. C.; Alkilany, A. M.; Huang, X.; Murphy, C. J.; El-Sayed, M. A. *Chem. Soc. Rev.* **2012**, *41*, 2740.
(18) Haruta, M. *CATTECH* **2002**, *6*, 102.
(19) Stratakis, M.; García, H. *Chem. Rev.* **2012**, *112*, 4469.
(20) Saha, K.; Agasti, S. S.; Kim, C.; Li, X.; Rotello, V. M. *Chem. Rev.* **2012**, *112*, 2739.
(21) Jans, H.; Huo, Q. *Chem. Soc. Rev.* **2012**, *41*, 2849.
(22) Dondapati, S. K.; Sau, T. K.; Hrelescu, C.; Klar, T. A.; Stefani, F. D.; Feldmann, J. *ACS Nano* **2010**, *4*, 6318.
(23) Mattox, T. M.; Bergerud, A.; Agrawal, A.; Milliron, D. J. *Chem. Mater.* **2014**, *26*, 1779.
(24) Liu, X.; Swihart, M. T. *Chem. Soc. Rev.* **2014**, *43*, 3908.
(25) Kriegel, I.; Jiang, C. Y.; Rodríguez-Fernández, J.; Schaller, R. D.; Talapin, D. V.; da Como, E.; Feldmann, J. *J. Am. Chem. Soc.* **2012**, *134*, 1583.
(26) Kriegel, I.; Rodríguez-Fernández, J.; Wisnet, A.; Zhang, H.; Waurisch, C.; Eychmüller, A.; Dubavik, A.; Govorov, A. O.; Feldmann, J. *ACS Nano* **2013**, *7*, 4367.
(27) Comin, A.; Manna, L. *Chem. Soc. Rev.* **2014**, *43*, 3957.
(28) Luther, J. M.; Jain, P. K.; Ewers, T.; Alivisatos, A. P. *Nat. Mater.* **2011**, *10*, 361.
(29) Hsu, S.-W.; On, K.; Tao, A. R. *J. Am. Chem. Soc.* **2011**, *133*, 19072.
(30) Lounis, S. D.; Runnerstrorm, E. L.; Llordes, A.; Milliron, D. J. *J. Phys. Chem. Lett.* **2014**, *5*, 1564.
(31) Manthiram, K.; Alivisatos, A. P. *J. Am. Chem. Soc.* **2012**, *134*, 3995.
(32) Lounis, S. D.; Runnerstrom, E. L.; Bergerud, A.; Nordlund, D.; Milliron, D. J. *J. Am. Chem. Soc.* **2014**, *136*, 7110.
(33) Neyshtadt, S.; Kriegel, I.; Rodríguez-Fernández, J.; Hug, S.; Lotsch, B.; Da Como, E. *Nanoscale* **2015**, *7*, 6675.
(34) Zhao, Y. X.; Pan, H. C.; Lou, Y. B.; Qiu, X. F.; Zhu, J. J.; Burda, C. *J. Am. Chem. Soc.* **2009**, *131*, 4253.
(35) Dorfs, D.; Hartling, T.; Miszta, K.; Bigall, N. C.; Kim, M. R.; Genovese, A.; Falqui, A.; Povia, M.; Manna, L. *J. Am. Chem. Soc.* **2011**, *133*, 11175.
(36) Balitskii, O. A.; Sytnyk, M.; Stangl, J.; Primetzhofer, D.; Groiss, H.; Heiss, W. *ACS Appl. Mater. Interfaces* **2014**, *6*, 17770.
(37) Li, W.; Zamani, R.; Rivera-Gil, P.; Pelaz, B.; Ibáñez, M.; Cadavid, D.; Shavel, A.; Álvarez-Puebla, R. A.; Parak, W. J.; Arbiol, J.; Cabot, A. *J. Am. Chem. Soc.* **2013**, *135*, 7098.
(38) Jain, P. K.; Manthiram, K.; Engel, J. H.; White, S. L.; Faucheaux, J. A.; Alivisatos, A. P. *Angew. Chem., Int. Ed.* **2013**, *52*, 13671.
(39) Kriegel, I.; Wisnet, A.; Kandada, A. R. S.; Scotognella, F.; Tassone, F.; Scheu, C.; Zhang, H.; Govorov, A. O.; Rodríguez-Fernández, J.; Feldmann, J. *J. Mater. Chem. C* **2014**, *2*, 3189.
(40) Rivest, J. B.; Jain, P. K. *Chem. Soc. Rev.* **2013**, *42*, 89.
(41) Beberwyck, B. J.; Surendranath, Y.; Alivisatos, A. P. *J. Phys. Chem. C* **2013**, *117*, 19759.
(42) Hessel, C. M.; Pattani, V. P.; Rasch, M.; Panthani, M. G.; Koo, B.; Tunnell, J. W.; Korgel, B. A. *Nano Lett.* **2011**, *11*, 2560.
(43) Tian, Q.; Jiang, F.; Zou, R.; Liu, Q.; Chen, Z.; Zhu, M.; Yang, S.; Wang, J.; Wang, J.; Hu, J. *ACS Nano* **2011**, *5*, 9761.
(44) Ku, G.; Zhou, M.; Song, S.; Huang, Q.; Hazle, J.; Li, C. *ACS Nano* **2012**, *6*, 7489.
(45) Liu, X.; Law, W. C.; Jeon, M.; Wang, X. L.; Liu, M. X.; Kim, C.; Prasad, P. N.; Swihart, M. T. *Adv. Healthcare Mater.* **2013**, *2*, 952.
(46) Ding, X.; Liow, C. H.; Zhang, M.; Huang, R.; Li, C.; Shen, H.; Liu, M.; Zou, Y.; Gao, N.; Zhang, Z.; Li, Y.; Wang, Q.; Li, S.; Jiang, J. *J. Am. Chem. Soc.* **2014**, *136*, 15684.
(47) Liu, X.; Lee, C.; Law, W. C.; Zhu, D. W.; Liu, M. X.; Jeon, M.; Kim, J.; Prasad, P. N.; Kim, C.; Swihart, M. T. *Nano Lett.* **2013**, *13*, 6298.

DOI: 10.1021/jacs.5b05337
J. Am. Chem. Soc. 2015, 137, 11666–11677

(48) Xia, Y.; Nguyen, T. D.; Yang, M.; Lee, B.; Santos, A.; Podsiadlo, P.; Tang, Z.; Glotzer, S. C.; Kotov, N. A. *Nat. Nanotechnol.* **2011**, *6*, 580.
(49) García de Abajo, F.; Howie, A. *Phys. Rev. B: Condens. Matter Mater. Phys.* **2002**, *65*, 115418.
(50) García de Abajo, F. J.; Howie, A. *Phys. Rev. Lett.* **1998**, *80*, 5180.
(51) Johnson, P. B.; Christy, R. W. *Phys. Rev. B* **1972**, *6*, 4370.
(52) Mansour, B. A.; Demian, S. E.; Zayed, H. A. *J. Mater. Sci.: Mater. Electron.* **1992**, *3*, 249.
(53) Palik, E. D. *Handbook of Optical Constants of Solids*; Academic Press: New York, 1985.
(54) Kriegel, I.; Rodríguez-Fernández, J.; Da Como, E.; Lutich, A. A.; Szeifert, J. M.; Feldmann, J. *Chem. Mater.* **2011**, *23*, 1830.
(55) Gordon, T. R.; Schaak, R. E. *Chem. Mater.* **2014**, *26*, 5900.
(56) Ye, X.; Reifsnyder Hickey, D.; Fei, J.; Diroll, B. T.; Paik, T.; Chen, J.; Murray, C. B. *J. Am. Chem. Soc.* **2014**, *136*, 5106.
(57) Liu, X.; Wang, X.; Zhou, B.; Law, W.-C.; Cartwright, A. N.; Swihart, M. T. *Adv. Funct. Mater.* **2013**, *23*, 1256.
(58) Zhu, D.; Tang, A.; Ye, H.; Wang, M.; Yang, C.; Teng, F. *J. Mater. Chem. C* **2015**, *3*, 6686.

DOI: 10.1021/jacs.5b05337
J. Am. Chem. Soc. 2015, 137, 11666−11677